

Augmented pyramidal photonic crystals for thin silicon photovoltaics

GRIFFIN SCHWARTZ* AND SAJEEV JOHN

University of Toronto Department of Physics, 60 St. George Street, Toronto, Ontario, M5S 1A7, Canada

*griffin.schwartz@utoronto.ca

Abstract: Wave-interference-based light trapping with photonic crystal structures offers a promising avenue for improving the power conversion efficiency of crystalline silicon solar cells beyond the current world record of 27.3%. Recent research on such devices has focused on structures with wet-etched inverted pyramidal pores. Using finite-difference time-domain simulations of Maxwell's equations, we demonstrate the remarkable robustness of this architecture and that in previously optimized 15 micron thick photonic crystal cells, light absorption can be further improved by 0.6% by slightly modifying the pore shape from a pyramid to that of a "golf-tee".

© 2025 Optica Publishing Group under the terms of the [Optica Open Access Publishing Agreement](#)

1. Introduction

Thin silicon film photonic crystal (PhC) solar cells offer a new paradigm for solar energy harvesting through wave-interference based light trapping effects. PhCs are artificial structures that have a spatially periodic dielectric function $\epsilon(\mathbf{r}, \omega)$. Such structures can exhibit strong light trapping effects such as slow light [1] or parallel-to-interface refraction (PIR), whereby normally incident light is bent almost 90° upon entering the material [2]. Slow light and PIR enhance light absorption by increasing light's dwell-time in the device: slow light modes travel more slowly, and PIR modes have a longer average path length due to being directed along the length and width of the cell, rather than its depth. In silicon PhC solar cells, a micron scale periodicity is desirable in order to create strong light trapping effects for infrared light. Silicon stands to gain the most in this wavelength range because it suffers from a weak intrinsic ability to absorb this light due to its indirect bandgap [3–5]. If PhC based thin silicon solar cells are to one day be used for large scale power generation, it is essential to optimize light absorption in these PhC structures.

Developing solar cells for wide-scale power generation requires a delicate balancing of many different constraints, some of which are in direct opposition to each other. Generally, such solar panels must be clean, scalable to mass production, and efficient. Silicon solar cells currently represent over 90% of the market [6–8] because they presently achieve the best balance of these criteria: silicon is much cleaner [6], more abundant [9] than, and cheaper to process [2] than direct bandgap semiconductors such as CdTe and GaAs. Silicon's weak absorption of infrared light due to its indirect bandgap has been overcome by using relatively thick layers of light absorbing materials, on the order of 100s of micrometers thick [7], compared to around 3 micrometers for thin cells made from other semiconductors such as CdTe [10]. In designing thin, silicon based PhC solar cells, the hope is to achieve a best-of-both worlds device that can benefit from the material advantages of silicon and the technological advantages of requiring only a thin light absorbing layer. Thinner devices suffer from less charge carrier recombination because the photo-excited charges have a smaller distance to travel to reach the contacts [11]. This also allows for less stringent requirements on material purity, which can help lower fabrication costs.

These devices' ability to absorb sunlight is characterized by the maximum available photocurrent density J_{MAPD} . This is the current that the cell would generate if every single absorbed photon

contributed exactly one charge carrier to the current. It is given by:

$$J_{\text{MAPD}} = \int_{\lambda_{\text{min}}}^{\lambda_{\text{max}}} e \left(\frac{\lambda}{hc} I(\lambda) \right) A(\lambda) d\lambda, \quad (1)$$

where e , h , and c are respectively the (positive) elementary charge, Planck's constant, and the speed of light. $I(\lambda)$ is the solar intensity spectrum, and $A(\lambda)$ is the absorption spectrum of the solar cell. e , h , c , and λ are organized to emphasize the physically relevant quantities under consideration. Fundamentally, solar light absorption is characterized by the total number of solar photons that the device can absorb per unit time. $\frac{\lambda}{hc} I(\lambda)$ is the photon number per unit area per unit time with which the sun irradiates the device. The device then absorbs a fraction $A(\lambda)$ of these incident photons. The factor of e then converts this quantity into a current density. To standardize MAPD comparisons, $I(\lambda)$ is taken to be the AM1.5G spectrum, which is the solar intensity spectrum under average conditions for the contiguous 48 states of the United States [12,13]. There are various sharp dips in the AM1.5G spectrum. These are due to resonant absorption of light by various chemical species in the atmosphere. The dips at around 750 nm and 950 nm are due to resonant rotational and vibrational modes of H₂O [14,15]. In this paper, we calculate J_{MAPD} between 300 nm and 1160 nm for the purposes of comparing structures, and for a select few structures it is calculated up to 1190 nm. Silicon's room temperature band gap is 1.12eV [5], which corresponds to a photon wavelength of 1107nm. 1160 nm is a sufficiently large cutoff wavelength to capture absorption through the exponentially suppressed Urbach tail and adequately characterize the structures' ability to absorb sunlight.

Previous theoretical studies of PhC silicon solar cells have revealed possible power conversion efficiencies of up to 31% [16], which approaches the thermodynamic efficiency limit of 32.33% for single junction silicon solar cells [17], and greatly surpassing the current world record efficiency of 27.3% for crystalline silicon solar cells [18,19]. All of this is while simultaneously reducing thickness by an order of magnitude compared to both the silicon solar cells that are available on the market today and to the state-of-the-art single junction silicon solar cells, including the cell that achieved the 27.3% world record [19,20]. This is possible because these state-of-the-art cells do not employ optimized photonic crystal texturing for wave interference-based light-trapping. Achieving an improved total efficiency with a thin-film enables light-weight, flexible solar cells that can be coated on building surfaces, vehicles, and even clothing.

In silicon PhC cells, periodicity in the dielectric function is achieved by etching away silicon from the top surface in a regular pattern. The etching can be performed with wet chemical solutions like KOH [21,22], or through reactive ion (plasma) beams [23]. The surface of the silicon slab is selectively exposed to the etching agent through means of a mask: a masking agent is deposited on to the top of the slab, and then holes are ablated in the mask with the desired periodicity for the PhC structure. Only the silicon exposed by these holes is then etched away, and then the mask is removed, leaving behind the periodic pattern of pores that constitutes the PhC.

The ablation and etching processes are key components of the overall cost and throughput of the manufacturing of PhC structures. Ablation can be done with standard or Deep UV photolithography [21–23], which ablates the holes in parallel but requires vacuum conditions. Direct laser writing is a serial ablation method that can be performed at room conditions which consists of moving the laser beam across the surface of the silicon with the laser pulses ablating the necessary holes [21,24]. There has already been experimental work seeking to improve the throughput of this method, including optimizing the beam profile to reduce the tracking tolerance and allow for faster beam movement [24]. This method has been proposed to be used in conjunction with Galvano-mirror scanning to achieve further increases in beam movement speed [25].

Recent work in optimizing silicon-based PhC solar cells has focused on PhC structures with inverted pyramidal pore shapes because this shape is both relatively easy to etch and has desirable

light trapping properties [21]. While conical pores have also demonstrated strong light trapping effects [26–28], they are harder to fabricate. The inverted pyramid shape arises naturally during a KOH wet-etch, whereas conical pores require more involved processes such as etching stacks of cylindrical excavations with successively smaller diameters [29]. A J_{MAPD} of $41.79 \frac{\text{mA}}{\text{cm}^2}$ in the 300–1200 nm range has been measured experimentally on a $10\mu\text{m}$ thick inverted pyramid pore PhC [26], whereas a recent world record thick-silicon solar cell with a power conversion efficiency of 26.81% had $J_{\text{MAPD}} = 41.16 \frac{\text{mA}}{\text{cm}^2}$ with a $130\mu\text{m}$ thick layer of silicon [20]. Furthermore, numerical studies have suggested that J_{MAPD} of the $10\mu\text{m}$ thick inverted pyramid PhC can go as high as $43.59 \frac{\text{mA}}{\text{cm}^2}$ in the 300–1200 nm range with idealized anti-reflection coatings [30]. These thinner cells could result in improved power conversion efficiency through both the increase of the total light absorbed, and the reduction in charge carrier recombination that accompanies thinner layers of light absorbing material.

There has been much research into optimizing PhCs with inverted pyramidal pores by optimizing characteristics of the cell such as lattice constant and overall cell thickness [16,30,31]. In this paper, we seek to optimize light absorption for thin film silicon PhC structures by considering changes to the shape of the pore itself by considering pore shapes that are different, but similar, to the inverted pyramid. The new, experimentally accessible, pore shapes under consideration are that of a golf-tee, upright pyramids, and inverted pyramidal pores of different depths. These shapes are chosen because previous works have already demonstrated that it is feasible to achieve these pore shapes, and because their optical properties have yet to be studied.

The golf-tee shape has been observed when using Al_2O_3 as a masking agent during the dry etch process (as opposed to chromium) [32]. Al_2O_3 is preferable as a masking agent because this material is already present in the contacts of the solar cell, whereas chromium should not be present in the final product. This means that the chromium mask must be completely washed away, and any remaining chromium atoms serve as impurities that increase the rate of charge carrier recombination, reducing the performance of the cell [24,32]. We numerically model the light trapping capabilities of the cells resulting from such an Al_2O_3 mask to determine if these structures would still be good candidates for PhC solar cells with strong light trapping properties, or if these shape changes significantly hamper the wave-interference-based light trapping effects we desire in these devices.

Upright pyramids can occur during the etching process when holes are missing in the etching mask. As the mask is removed, some silicon is removed from the top of the slab as well. When a hole is missing in the mask, the silicon underneath the missing hole is not removed during the wash. This silicon left at the original, pre-wash height then constitutes an upright pyramid with respect to the new top-surface layer that remains post-wash [24,33].

Lastly, we considered a change in the depth of the pyramidal pore. The wet etching processes described above results in pyramidal pores because the etching agent removes the (100) plane of silicon, exposing the (111) plane. The angle between these two planes is then fixed at 54.7° , and so the depth h of the pore is determined by the side length L of the base of the pyramidal pore by:

$$h = \tan(54.7^\circ) \frac{L}{2}. \quad (2)$$

It may be possible to achieve a different side wall angle by other dry-etching methods [21]. We calculate J_{MAPD} for PhC with inverted pyramid pores of different side wall angles to investigate if solar light absorption could be further enhanced by intentionally changing the side wall angle.

It is worth highlighting that these modifications to the inverted pyramidal pore shapes were observed in experimental studies that were not only seeking to improve the performance of silicon based PhC solar cells, but were also seeking to improve the throughput of the production of such cells [21,24,32]. Assessing the optical performance of the resulting pore shapes is therefore a crucial aspect of improving the throughput of silicon-based PhC solar cells to bring the promise of their low-cost mass-production to reality.

Typical light trapping architectures for thick silicon cells, based on the principles of ray optics, include large scale (compared to the wavelengths of light) inverted pyramids [34,35], and random texturing [30,34]. In this context, it has become standard practice to compare silicon cells' light absorption to the Lambertian Limit: an estimate of MAPD based on an idealized Lambertian scattering ray optics picture. In some instances, this model has been used to suggest a supposed theoretical upper limit on the performance of single-junction silicon solar cells [36]. This model assumes that normally impinging light rays (unrealistically) penetrate the cell with no reflective losses and are scattered randomly off the normal according to a $\cos \theta$ probability distribution (where θ is the angle the ray makes with the normal of the slab). This distribution characterizes diffuse Lambertian light scattering. The rays are then completely reflected by a perfect electric conductor on the back surface of the cell and (unrealistically) either completely escape or undergo total internal reflection at the top surface, whereby they are once again randomly scattered in an independent scattering event, repeating the process until being scattered into an angle that allows for the ray to escape. Wave interference effects are completely ignored. Under these assumptions, the average path length of a light ray in a cell of thickness L , with index of refraction n , is $4n^2L$. $A(\lambda)$ is then calculated as the ratio of the light's absorption rate (calculated using experimental data for the absorption length) to the sum of its absorption and escape rates.

The underlying assumptions of the Lambertian model should highlight that it is not a fundamental limit on the amount of light a solar cell can absorb. As mentioned above, this model completely neglects the wave properties of light by treating light transmission and reflection as binary processes. Furthermore, light need not scatter according to a $\cos \theta$ distribution. In fact, an important part of wave-interference-enabling structures is to create scattering distributions favouring larger values of θ .

In this paper, we compare the J_{MAPD} of the new structures with that of the standard inverted pyramid shaped pores, with the Lambertian limit J_{MAPD} , denoted by $J_{\text{MAPD}}^{\text{Lamb}}$, and with the J_{MAPD} of a hypothetical perfect absorber. This reveals precisely how the proposed shapes affect light absorption in the context of widely-studied architectures. Numerical and experimental studies have already demonstrated that the standard inverted pyramid silicon PhC structures can surpass $J_{\text{MAPD}}^{\text{Lamb}}$ [16,26,30]. Our study further underscores the nearly ideal nature of these wet-etched structures. Since the light trapping phenomena we desire in PhC solar cells result from the wave interference of light, these structures must be numerically modelled with precise solutions to Maxwell's equations.

2. Methods

Absorption spectra are calculated numerically with finite-difference time-domain (FDTD) method on a three dimensional structure, implemented with the most recent version of the open source software Electromagnetic Template Library (EMTL) [37]. In the simulations, we define a single unit cell of the PhC structure and impose periodic boundary conditions in the x and y directions to achieve the effect of translational symmetry in $\epsilon(\mathbf{r}, \omega)$. The simulation boundaries in the z direction are each set to be a Perfectly Matched Layer (PML) to ensure the simulated structure has finite extent along the light's direction of incidence.

The absorption spectrum $A(\lambda)$ is inferred from $A = 1 - R - T$. Reflection and transmission spectra are tabulated using flux planes. The reflection flux plane is placed in the scattered field region, above the structure, and the transmission plane is placed underneath the structure (where the top of the structure is understood to be the side struck by the impinging light). The total electromagnetic flux (the energy per unit time per unit area, denoted with Φ) that crosses the reflection plane during the simulation is calculated, and then the reflection coefficient is calculated from:

$$R = \frac{\Phi_{\text{through reflection plane}}}{\Phi_{\text{incident}}}. \quad (3)$$

The same is done for the transmission coefficient with the flux through the transmission plane. The impinging light pulse in EMTL is a Berenger pulse of the form:

$$E(t) = \begin{cases} E_0 \cdot (t - t_0) \cdot e^{-\left(\frac{t-t_0}{t_w}\right)^2} & , \text{ for } |t - t_0| \leq T \\ 0 & , \text{ for } |t - t_0| > T, \end{cases} \quad (4)$$

with $E_0 = 1$ in EMTL units of electric field (specific unit is unimportant because the only outputs we concern ourselves with are the dimensionless reflection and transmission coefficients), $t_0 = 0.5$ light-microns, $t_w = 0.1$ light-microns (which is the width of the pulse), and $T = 2.5$ light-microns. A light-micron is the time it takes light to traverse one micron, approximately 3.34×10^{-15} seconds. The chosen parameters result in a pulse that is sufficiently narrow in the time domain to be wide enough in the frequency domain to cover the wavelength range of interest for the device.

Our reference inverted pyramid PhC structure has a cell thickness of $15\mu\text{m}$ with lattice constant $3.1\mu\text{m}$. Unless otherwise stated, the simulated structures have a mesa (flat region between edges of pyramids) of 30 nm, and a three layer anti-reflection coating (ARC) consisting of (from top to bottom) an 80 nm layer of SiO_2 ($n=1.47$), a 40 nm layer of SiN ($n=1.9$), and a 20 nm layer of Al_2O_3 ($n=1.77$). We place a 100 nm thick passivating buffer layer of SiO_2 (glass) on the bottom of the cell, and the charge collecting contacts underneath the passivating layer. The presence of a buffer layer between the silicon and metal contact increases reflection off of the bottom of the structure [38], which allows for the contact to be modelled as a perfect electric conductor. Any material present in the cell other than silicon is modelled with a frequency-independent index of refraction with no absorption. The frequency independence of refraction is a valid approximation in these simulations because these materials' index of refraction varies by no more than 0.1 over the wavelength range of interest. We verified this by performing a simulation on the optimized golf-tee structure with the index of refraction for each ARC layer reduced by the maximum amount by which that material varies over the entire wavelength range, and calculated no change to the J_{MAPD} of $43.05 \frac{\text{mA}}{\text{cm}^2}$ over the 300-1190 nm range. Since this change to the indices of refraction necessarily constitutes a larger change to the frequency-independent refractive index than implementing the full frequency-dependent form, yet still resulted in no calculated change to the J_{MAPD} , we may conclude that modelling these materials with a frequency-independent index of refraction is a valid approximation for these numerical methods.

Silicon's complex and frequency-dependent dielectric function [4] is implemented in the FDTD scheme by fitting it to a series of modified Lorentz functions, of the form [39]:

$$\epsilon(\omega) = \epsilon_\infty + \sum_{j=1}^p \frac{\Delta\epsilon_j (\omega_j^2 - i\gamma_j'\omega)}{\omega_j^2 - 2i\gamma_j\omega - \omega^2}. \quad (5)$$

Each modified Lorentz function has four fitting parameters: $\Delta\epsilon_j$, ω_j , γ_j , γ_j' . The values of each of these parameters in a fit, along with the number of fitting terms used, p , and the wavelength range over which the dielectric function is fit, do not necessarily have a physical meaning. They are simply chosen to achieve a function that resembles the true dielectric function of silicon as closely as possible, over as wide a wavelength range as possible. For our simulations, we have fit the dielectric function of silicon in three intervals: $[300\text{nm}, 1030\text{nm}]$, $[1030\text{nm}, 1160\text{nm}]$, and $[1160\text{nm}, 1190\text{nm}]$. EMTL does not accept piece-wise definitions for the dielectric function, so each wavelength range requires a distinct simulation. This is the cause of the sharp change in the calculated absorption spectra at 1030 nm. For more details on the fits used in the simulations, and the procedure we followed for obtaining these fits, see [Supplement 1](#) online. The fitting coefficients used in the simulations are presented in Supplementary Table S1.

The golf-tee pore takes the shape of a pyramid that has been sliced in two, with the two parts joined together by a rectangular prism (the stem). This is illustrated in Fig. 1. The pore has two independent parameters f and h_b that characterize, respectively, the width and length of the stem. f is the ratio between the width of the stem and the width of the base of the pyramid (since the width of the pyramid at a given point depends uniquely on the height of that point, f also determines how deep in the pyramidal pore the stem begins) and h_b is the length of the stem, in microns. We consider 14 architectures of the golf-tee pore, chosen from $f = [0.1, 0.15, 0.2, 0.25]$ and $h_b = [1.00\mu\text{m}, 1.25\mu\text{m}, 1.50\mu\text{m}]$, as well as ones with $f = 0.3$ and $h_b = 1.5\mu\text{m}$, and $f = 0.25$ and $h_b = 1.75\mu\text{m}$. These parameters were chosen because they correspond to golf-tee sizes that appear similar to the features in recent fabrication studies [32].

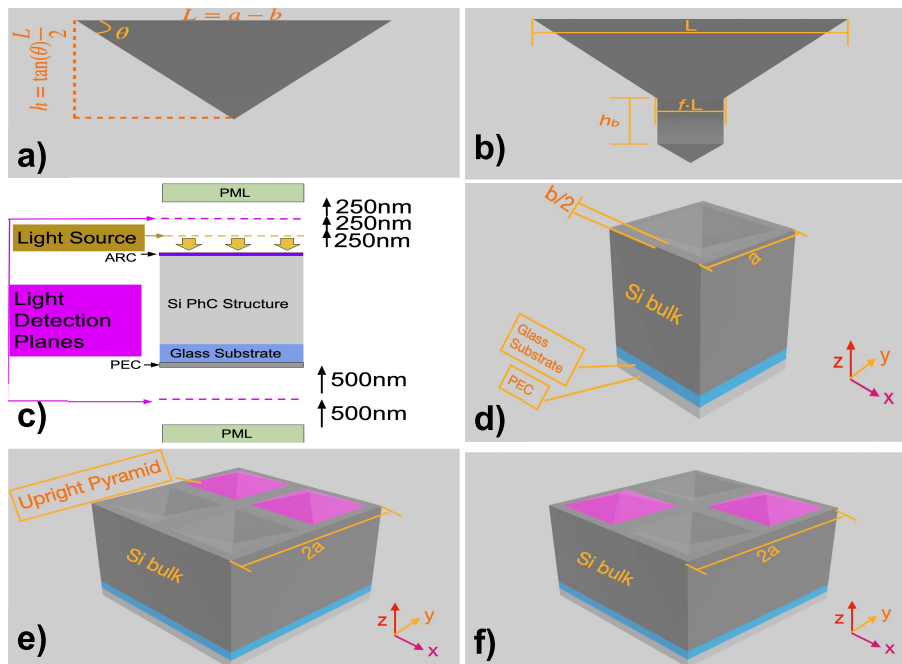


Fig. 1. The PhC architectures under consideration. **(a)** The standard inverted pyramid pore shape. The base side length is determined by the lattice constant a of the PhC structure and the mesa width (flat region between pores) b . The side wall angle then determines the depth of the pyramidal pore, following Eq. (2). **(b)** The golf-tee pore, whose key features are the width and depth of the stem, characterized by parameters f and h_b . **(c)** Sketch of the computational domain region in the FDTD simulations. The Perfectly Matched Layers (PMLs) are parallel to the xy plane and terminate the domain, while periodic boundary conditions are imposed at the boundary domains parallel to the xz and yz planes. The anti-reflective coating (ARC) at the top of the cell serves to minimize reflective losses, and the charge collecting contacts under the glass buffer layer block all transmission of light through the cell. The contacts are modelled as a perfect electric conductor (PEC). This is achieved numerically by setting the material to have a frequency-independent index of refraction of 10^8 . The dashed lines represent non-physical objects in the simulation (i.e. they do not scatter or absorb light). **(d)** A unit cell for the reference inverted pyramid PhC structure. **(e)** The PhC with aligned upright pyramids. Two unit cells are shown to highlight the relative arrangement of the pyramids, but in our calculations we only use one unit cell. The upright pyramids are coloured differently for clarification, but they consist of the same silicon material as the rest of the cell. **(f)** A unit cell of the PhC structure with staggered upright pyramids, forming a checkerboard pattern of upright and inverted pyramids.

For PhC cells with upright pyramids, we considered a 1:1 ratio of upright to inverted pyramids, as well as a cell with all upright pyramids. For the former, there are two possible ways to arrange such a PhC structure: the upright pyramids can be aligned in rows, or staggered to form a checkerboard pattern. Only a 1:1 ratio is considered because it results in the smallest possible unit cell for a structure with two different types of pores.

Variations in pore height are considered by changing the angle that the side walls of the pyramid make with the flat surface of the cell, which affects the depth of the pore according to Eq. (2). 54.7° is the standard value, and to consider physically realistic changes we consider angles that differ by at most around 15° . The considered angles are 40° , 45° , 50° , 60° , 65° , and 70° .

3. Results and discussion

There are three reference structures to which we compare our modified PhC structures: a Lambertian absorber, the standard wet-etched inverted pyramid PhC structure, and a hypothetical perfect absorber that has $A(\lambda) = 1$ for all λ . J_{MAPD} of a perfect absorber is the total available solar photocurrent density in a given wavelength range. It is $39.80 \frac{\text{mA}}{\text{cm}^2}$ in the 300-1030 nm range, $5.04 \frac{\text{mA}}{\text{cm}^2}$ in the 1030-1160 nm range, and $1.19 \frac{\text{mA}}{\text{cm}^2}$ in the 1160-1190 nm range, for a total available sunlight of $46.03 \frac{\text{mA}}{\text{cm}^2}$ in the 300-1190 nm range.

$J_{\text{MAPD}}^{\text{Lamb}}$ for a 15 μm silicon slab is $38.75 \frac{\text{mA}}{\text{cm}^2}$ in the 300-1030 nm range (97.4% of available sunlight), $1.81 \frac{\text{mA}}{\text{cm}^2}$ in the 1030-1160 nm range (36.0% of available sunlight), and $0.01 \frac{\text{mA}}{\text{cm}^2}$ in the 1160-1190 nm range (0.8% of available sunlight), for a total MAPD of $40.57 \frac{\text{mA}}{\text{cm}^2}$ in the 300-1190 nm range (88.1% of available sunlight). Here, silicon's poor intrinsic absorption of infrared light is clear from the precipitous drop-off of the fraction of total sunlight absorbed as the wavelength ranges shift further into the infrared spectrum.

The reference wet-etched inverted pyramidal pore PhC structure (15 μm thick, $a = 3.1 \mu\text{m}$, 3 layer ARC) has a calculated $J_{\text{MAPD}} = 38.51 \frac{\text{mA}}{\text{cm}^2}$ in the 300-1030 nm range (96.8% of total sunlight), $J_{\text{MAPD}} = 3.23 \frac{\text{mA}}{\text{cm}^2}$ in the 1030-1160 nm range (64% of available sunlight), and $J_{\text{MAPD}} = 0.68 \frac{\text{mA}}{\text{cm}^2}$ in the 1160-1190 nm range (57.1% of total sunlight), for a total $J_{\text{MAPD}} = 42.42 \frac{\text{mA}}{\text{cm}^2}$ in the 300-1190 nm range (92.2% of total sunlight). Despite the PhC structure absorbing slightly less than the Lambertian limit in the 300-1030 nm range, the PhC is able to surpass the Lambertian limit over the broader spectrum due to its significantly enhanced absorption of infrared light. The inverted pyramidal pore shape effectively traps light in this wavelength range because it induces vortex-like flow of the Poynting vector [16]. Silicon's intrinsic ability to absorb infrared light is so weak that there are massive gains to be had by inducing strong infrared light trapping with the PhC's micron-scale features. This is evident in Fig. 2, where the Lambertian absorption limit falls off precipitously starting at 1000 nm. The Lambertian limit of $1.82 \frac{\text{mA}}{\text{cm}^2}$ in the 1030-1190 nm range corresponds to only 29.2% of the total available sunlight. The reference inverted pyramid PhC structure has a calculated $J_{\text{MAPD}} = 3.91 \frac{\text{mA}}{\text{cm}^2}$ in this range, which amounts to 62.8% of available sunlight. This is more than double the Lambertian limit MAPD in this wavelength range. These gains are sufficiently large to enable the cell to outperform the Lambertian limit even over the broader 300-1190 nm spectrum.

The sharp change at 1030 nm in the calculated absorption spectra of our considered architectures is due to the longer simulation times needed to achieve numerical convergence, which results in a higher frequency resolution. See Supplement 1 for a discussion on numerical convergence of FDTD simulations.

All of the calculated J_{MAPD} are presented in Table 1.

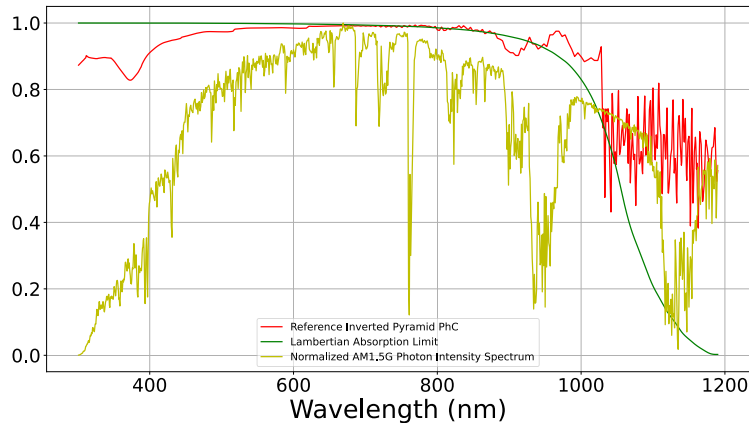


Fig. 2. Absorption spectra of the Lambertian limit and of the reference inverted pyramid PhC structure. The latter is obtained through FDTD solutions of Maxwell's equations. This absorption spectrum is the $A(\lambda)$ used to calculate J_{MAPD} in Eq. (1). The AM1.5G photon intensity spectrum ($\frac{\lambda}{hc}I(\lambda)$ in Eq. (1)), normalized by its maximum value, is overlaid. Light trapping effects at long wavelengths are essential for the PhC's ability to surpass $J_{\text{MAPD}}^{\text{Lamb.}}$: the PhC's light absorption begins to vastly surpass the Lambertian limit at around 1000 nm, in a wavelength range where the solar photon intensity still surpasses 60% of the solar peak intensity.

3.1. Golf-tee pore photonic crystal

12 out of the 14 considered architectures exhibit a calculated J_{MAPD} higher than the standard inverted pyramid pore shape, and all 14 of them surpass the Lambertian limit. The best performing golf-tee shape, with $f = 0.25$ and $h_b = 1.50\mu\text{m}$, had a J_{MAPD} that was 0.6% higher than the standard inverted pyramid shape, while the worst performing golf-tee shape only saw a reduction of 0.43%. This suggests that the inverted pyramidal pore shape is already nearly optimum for light absorption in thin silicon slabs. However, the golf-tee modification to the inverted pyramid shape offers a slight but noticeable enhancement in overall light absorption, while using a smaller volume of silicon. The golf-tee pores with $f = 0.3$ and $h_b = 1.50\mu\text{m}$, and $f = 0.25$ and $h_b = 1.75\mu\text{m}$ were added to verify that the the pore with $f = 0.25$ and $h_b = 1.50\mu\text{m}$ is in fact optimal.

In our numerical simulations, the best performing golf-tee PhC surpasses the reference structure's J_{MAPD} in both of the considered wavelength ranges of 300-1030 nm and 1030-1160 nm. As seen in Fig. 3, the golf-tee pore's improved J_{MAPD} in the 300-1030 nm range is due to its enhanced suppression of reflection from 390 nm to 650 nm.

This reflection suppression can perhaps be understood through a semi-ray optics scheme where the geometry of the light's path follows the laws of ray optics, but with the light undergoing partial reflection and transmission each time it impinges on the surface of the cell. In this model, the light undergoes specular reflection off of the surface of the cell, with the geometry of the pore dictating how many bounces the ray undergoes before being directed away from the cell. Since the fraction of the beam that transmits into the cell to be absorbed is the same on each ray reflection event, the geometry that induces the most number of light ray bounces before directing away the ray will have the strongest absorption [40]. Since the golf-tee pore is deeper than the reference inverted pyramid pore, its stronger anti-reflection properties at shorter wavelengths could be attributed to the golf-tee pore inducing more ray bounces.

Colour maps of the electric field intensity at the wavelengths of 950 nm and 1152 nm for the best performing golf-tee pore ($f = 0.25$ and $h_b = 1.5\mu\text{m}$) are presented in Fig. 4. The

Table 1. J_{MAPD} of all of the considered architectures

Structure	J_{MAPD} 300-1030 nm range $\left(\frac{\text{m}\Lambda}{\text{cm}^2}\right)$	J_{MAPD} 1030-1160 nm range $\left(\frac{\text{m}\Lambda}{\text{cm}^2}\right)$	J_{MAPD} 300-1160 nm range $\left(\frac{\text{m}\Lambda}{\text{cm}^2}\right)$
Lambertian Limit Absorber	38.75	1.81	40.56
Reference Inv. Pyramid Pore	38.51	3.23	41.74
Golf-Tee $f = 0.1$	$h_b = 1.00\mu\text{m}$	38.58	41.83
	$h_b = 1.25\mu\text{m}$	38.60	41.87
	$h_b = 1.50\mu\text{m}$	38.61	41.89
Golf-Tee $f = 0.15$	$h_b = 1.00\mu\text{m}$	38.54	41.75
	$h_b = 1.25\mu\text{m}$	38.56	41.86
	$h_b = 1.50\mu\text{m}$	38.54	41.79
Golf-Tee $f = 0.2$	$h_b = 1.00\mu\text{m}$	38.61	41.84
	$h_b = 1.25\mu\text{m}$	38.64	41.89
	$h_b = 1.50\mu\text{m}$	38.66	41.97
Golf-Tee $f = 0.25$	$h_b = 1.25\mu\text{m}$	38.30	41.60
	$h_b = 1.50\mu\text{m}$	38.65	3.34
	$h_b = 1.75\mu\text{m}$	38.58	41.93
Golf-Tee $f = 0.3$	$h_b = 1.50\mu\text{m}$	38.58	41.94
All Upright Pyramids	36.97	3.48	40.45
Aligned Upright Pyramids	37.50	3.28	40.78
Staggered Upright Pyramids	32.11	2.60	34.71
Inv. Pyramid - 40° Side Wall Angle	37.25	3.54	40.79
Inv. Pyramid - 45° Side Wall Angle	37.91	3.01	40.92
Inv. Pyramid - 50° Side Wall Angle	38.29	3.02	41.31
Inv. Pyramid - 60° Side Wall Angle	37.88	2.90	40.78
Inv. Pyramid - 65° Side Wall Angle	36.45	2.33	38.78
Inv. Pyramid - 70° Side Wall Angle	37.77	2.73	40.50
Hypothetical Perfect Absorber	39.80	5.04	44.84

absorption is proportional to the volume integral of the electric field intensity multiplied by the imaginary part of silicon's dielectric constant [27]. As seen in Fig. 3, the golf-tee pore has a local peak in absorption at 1152 nm but does not have such a peak at 950 nm. The colour maps at 1152 nm show the presence of many strongly localized regions of high electric field intensity arising from wave-interference. The light at 1152 nm is strongly trapped near the bottom of the structure. While 950 nm does not correspond to an isolated resonance peak in absorption, the structure still has a higher absorption coefficient at 950 nm than at 1152 nm because the imaginary part of silicon's dielectric constant is an order of magnitude larger at 950 nm compared to 1152 nm [4]. As silicon's intrinsic ability to absorb light decreases with increasing wavelength, wave-interference-based light trapping becomes crucial for absorption to occur.

3.2. Upright pyramids

The presence of any upright pyramids in the PhC structure results in a reduction in the calculated J_{MAPD} in the 300-1160 nm range. Replacing all of the inverted pyramids with upright pyramids results in a 3.1% reduction of J_{MAPD} , to fall just below the Lambertian limit of $40.56 \frac{\text{m}\Lambda}{\text{cm}^2}$. This is due to the large drop in the 300-1030 nm range, whereas the upright pyramid structure actually has

a larger J_{MAPD} in the 1030-1160 nm range. In particular, the upright pyramidal pore reflects much more light below 600 nm, as seen in Fig. 5(a). The 7.7% increase of J_{MAPD} in the 1030-1160 nm range, however, suggests that such structures could in fact be advantageous for devices such as infrared photodetectors that only require strong light trapping in long wavelength ranges.

The PhC with aligned upright pyramids suffers a smaller reduction in overall calculated J_{MAPD} compared to the PhC with all upright pyramids, for a 2.3% reduction that is still above the Lambertian limit. The PhC with staggered upright pyramids, however, suffers an extreme reduction in calculated J_{MAPD} . This checkerboard arrangement exhibits an overall decrease of 16.8% compared to all upright pyramids. The resultant MAPD falls well below the Lambertian limit. The calculated J_{MAPD} of these two structures (aligned or staggered upright pyramids) differs by 14.8% despite having the same amount of light absorbing material and the same ratio of inverted-to-upright pyramids. This reveals that the geometrical arrangement of the upright pyramids can have significant effects on the structure's ability to absorb sunlight.

The shape of the absorption spectrum for the PhC with staggered upright pyramids (the red curve in Fig. 5(b)) displays sharp resonances similar to those of an untextured silicon slab [27], but at longer wavelengths. The checkerboard structure has a lattice constant of $6.2\mu\text{m}$, which is about six times longer than any of the wavelengths of light under consideration. This periodicity may be too big to effectively trap light in the wavelength vicinity of 1000 nm. The PhC with aligned upright pyramids, on the other hand, has a lattice constant in one direction that is $3.1\mu\text{m}$ and $6.2\mu\text{m}$ in the other, which appears sufficient to retain some wave-interference-based light trapping effects at the wavelengths of interest.

3.3. Side wall angle

The side wall angle of 54.7° seen in the reference inverted pyramid PhC structure appears to be optimal for broadband light absorption. There are likely no gains to be made for solar energy conversion by changing the depth of the pyramidal pore.

Interestingly, the calculated J_{MAPD} in the 1030-1160 nm range in the PhC structure with an inverted pyramid side wall angle of 40° is $3.54 \frac{\text{m}\cdot\text{A}}{\text{cm}^2}$, which is the highest calculated J_{MAPD} in this range of any structure considered in this paper. This can be attributed to its strong absorption of light, compared to the reference structure, around 1030 nm as seen in Fig. 6. This shallower

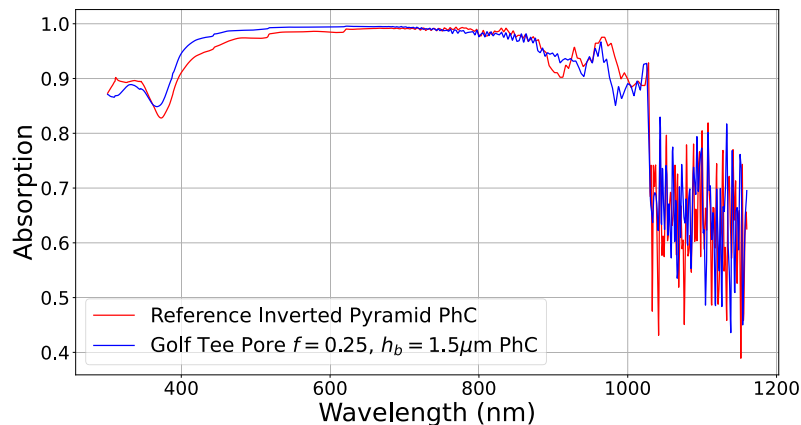


Fig. 3. Calculated absorption spectra of the best performing golf-tee ($f = 0.25$, $h_b = 1.5\mu\text{m}$) PhC and of the reference inverted pyramid PhC structures. The golf-tee pore PhC's higher absorption in the shorter wavelength range of about 390-650 nm suggests that this particular pore shape has enhanced anti-reflective properties at shorter wavelengths, while also slightly improving light trapping in the longer wavelength range.

inverted pyramidal pore PhC, like the upright pyramidal pore structure, could be relevant for devices such as infrared photodetectors.

3.4. Maximizing J_{MAPD} with an ideal PhC structure

Finally, we have applied our findings to numerically calculate J_{MAPD} of a PhC structure that is optimized for light trapping. We considered a golf-tee pore with $f = 0.25$, and $h_b = 1.5\mu\text{m}$, since, of all the structures considered in this paper, this was the one with the highest calculated J_{MAPD} in the 300-1160 nm range. We then reduced the mesa width from 30 nm to 5 nm, reduced the thickness of the Al_2O_3 ARC layer from 20 nm to 5 nm, and replaced the middle ARC layer of SiN ($n=1.9$) with SiC ($n=2.6$). We reduced the mesa width in the hopes that a smaller flat region between pyramids would improve light absorption by reducing specular reflection at the top surface. Replacing the middle ARC layer of SiN with SiC was done because SiC's index of refraction of 2.6 provides better index matching to that of silicon, whose lowest index of refraction in the considered wavelength range is around 3. We reduced the thickness of the bottom ARC layer of Al_2O_3 for the same reason, as it has $n = 1.77$, which provides poor index matching to silicon. The results of this J_{MAPD} optimization are presented in Table 2.

Numerical simulations on the above structure yield a J_{MAPD} that is 6.1% higher ($2.48 \frac{\text{mA}}{\text{cm}^2}$) than the Lambertian limit for a $15\mu\text{m}$ thick slab of silicon, and also represents an improvement

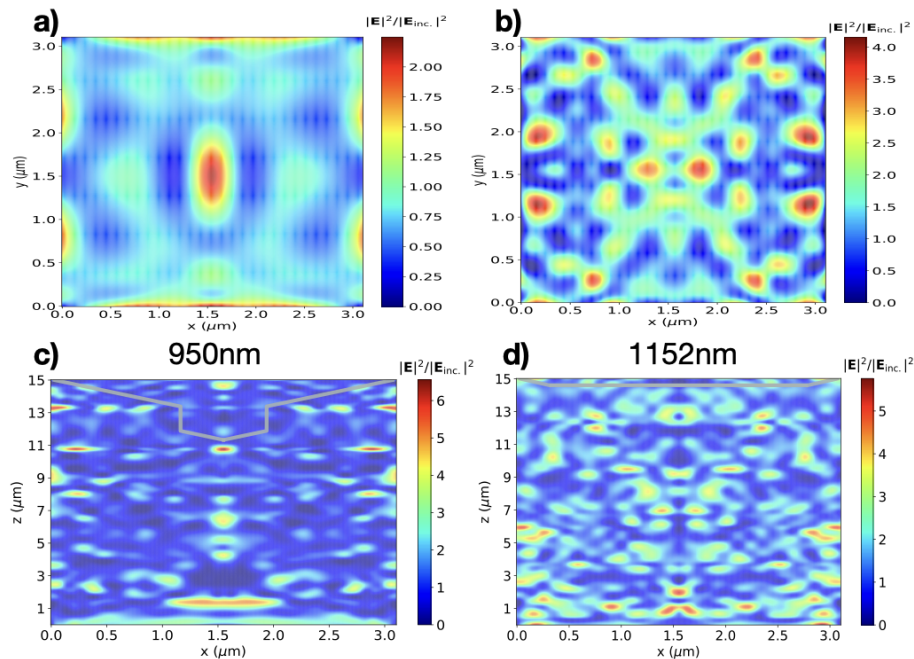


Fig. 4. Electric field intensity colour maps in various cut planes for the best performing golf-tee structure (with $f = 0.25$ and $h_b = 1.5\mu\text{m}$), taken at 950 nm (in **a** and **c**) and at 1152 nm (in **b** and **d**). The electric field intensities are normalized by the incident intensity at the wavelength of interest. **a**) xy -plane cut near the tip of the golf-tee pore ($z = 11\mu\text{m}$ in **c**), showing the electric field intensity at 950 nm. **b**) xy -plane cut near the bottom of the structure ($z = 3\mu\text{m}$ in **d**), showing the electric field intensity at 1152 nm. **c**) xz -plane cut through the centre of the unit cell at $y = 0.5a = 1.55\mu\text{m}$, showing the electric field intensity at 950 nm. The boundary of the pore is drawn in grey. **d**) xz -plane cut at $y = 0.1a$, showing the electric field intensity at 1152 nm. The boundary of the pore is drawn in grey.

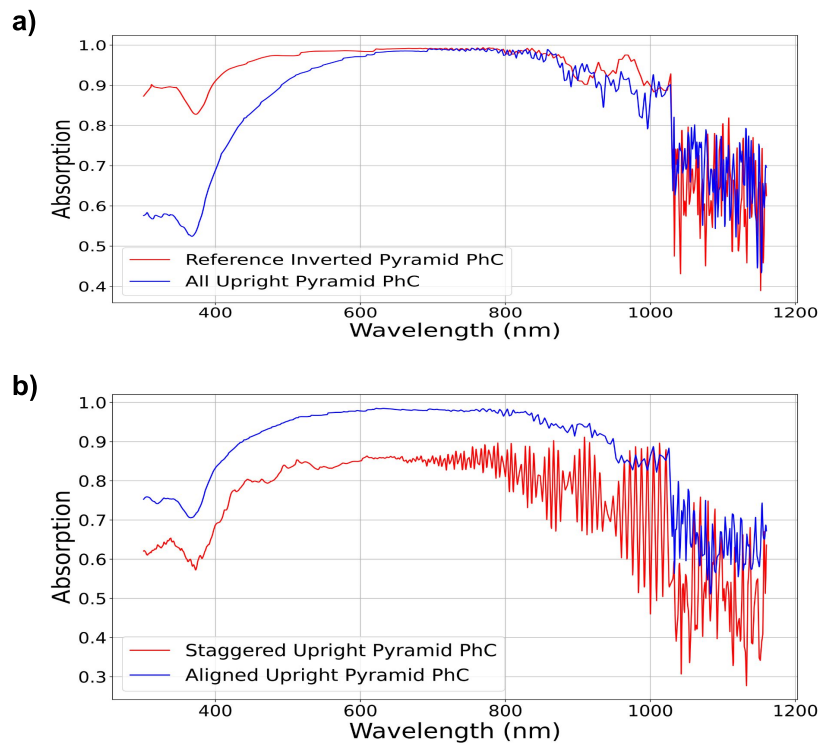


Fig. 5. The calculated absorption spectra of the PhC architectures with upright pyramids. **(a)** Calculated absorption spectra of the PhCs with upright pyramids (blue curve) and inverted pyramids (red curve). The upright pyramid PhC has enhanced light trapping in the infrared range at the cost of stronger reflection at shorter wavelengths, thus making for a worse device for broadband solar light absorption. **(b)** Absorption spectra of PhC structures with aligned (blue curve) or staggered (red curve) upright pyramids. Despite each having the same number of upright and inverted pyramids, the PhC with staggered upright pyramids was calculated to have a significantly lower J_{MAPD} .

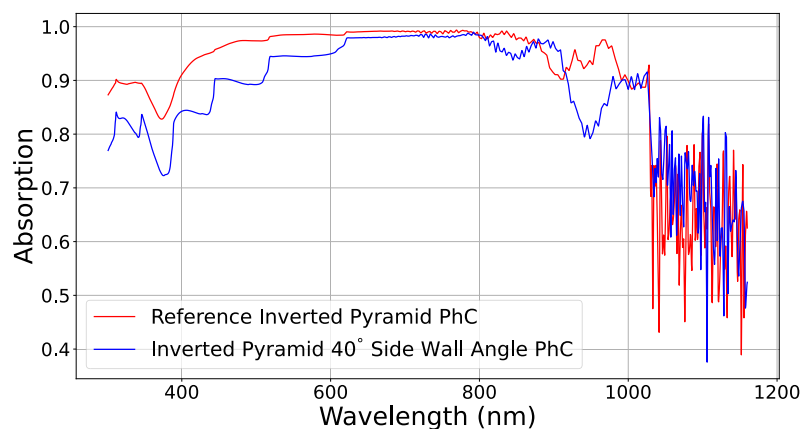


Fig. 6. Absorption spectra of inverted pyramid PhC structure with side wall angle of 40° or 54.7° (the unperturbed angle). Fortunately, the unperturbed angle of 54.7° is better suited for broad spectrum solar absorption, however changing the side wall angle to 40° improved J_{MAPD} in the 1030-1160 nm range by 9.6%.

Table 2. J_{MAPD} of the optimized PhC structure and the reference structures

Structure	J_{MAPD} 300-1030 nm range ($\frac{\text{mA}}{\text{cm}^2}$)	J_{MAPD} 1030-1160 nm range ($\frac{\text{mA}}{\text{cm}^2}$)	J_{MAPD} 1160-1190 nm range ($\frac{\text{mA}}{\text{cm}^2}$)	J_{MAPD} 300-1190 nm range ($\frac{\text{mA}}{\text{cm}^2}$)
Lambertian Limit Absorber	38.75	1.81	0.01	40.57
Reference Inv. Pyramid Pore	38.51	3.23	0.68	42.42
Optimized Golf-Tee Pore PhC	38.78	3.40	0.87	43.05
Hypothetical Perfect Absorber	39.80	5.04	1.19	46.03

of 1.5% ($0.63 \frac{\text{mA}}{\text{cm}^2}$) compared to the reference inverted pyramid pore PhC structure. Its overall calculated J_{MAPD} is 93.5% of the total available sunlight. The improved anti-reflection properties can be readily seen in Fig. 7, where the optimized structure has near perfect absorption from 400 nm to 600 nm. It has particularly strong absorption in the 1160-1190 range as well, where its J_{MAPD} improved by 27.9% compared to the reference inverted pyramidal pore PhC structure. This is especially useful in improving overall J_{MAPD} because the AM1.5G spectrum recovers from a particularly strong dip at these wavelengths, and there is more sunlight to absorb closer to 1200 nm than at 1100 nm.

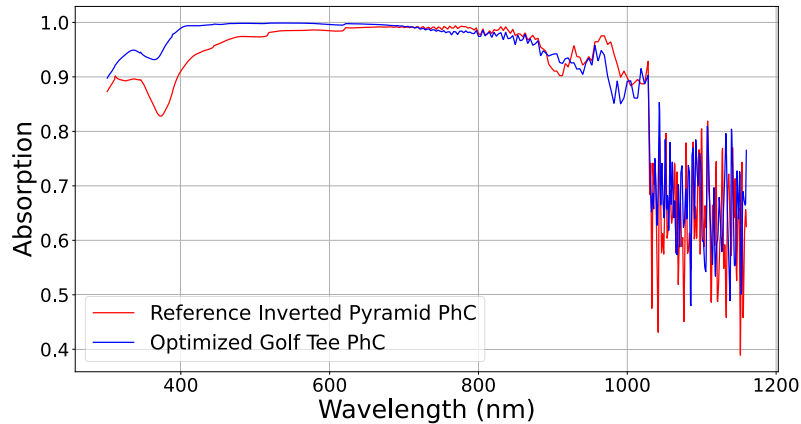


Fig. 7. Absorption spectrum of the optimized golf-tee PhC structure compared to the reference inverted pyramid structure. These numerical results suggest that the changes to the ARC and mesa width would have their intended effect of reducing reflective losses, as evidenced by the improved calculated absorption in the short wavelength range, in particular the slight flattening of the dip at the silicon band edge of 390 nm, and the near perfect absorption from 400 nm to around 620 nm.

4. Conclusion

The opportunity is apparent for improving the power conversion efficiency of silicon solar cells by exploiting the wave nature of light with photonic crystal structures. Whereas the current world record silicon cell has a power conversion efficiency of 27.3% [18,19], previous numerical studies on silicon photonic crystal cells have revealed the potential to reach 31% using inverted pyramidal pores on the surface of the silicon cell. This potential emerges from enhanced absorption of infrared sunlight using wave-interference light trapping. This enables the cells to be made an order of magnitude thinner than current world record cells, which results in further increases to efficiency through reduced Auger charge carrier recombination.

In this paper we considered three different changes to standard inverted pyramid pore architecture, which were motivated by fabrication methods. These consisted of: golf-tee pores (which were discovered using Al_2O_3 as a masking agent), alternating upright and inverted pyramids in the structure, and pyramidal pores with modified side-wall angles. Each of these were considered on $15\mu\text{m}$ thick cells with $3.1\mu\text{m}$ lattice constants. While improved absorption is found in specific wavelength ranges, the standard inverted pyramid architecture is remarkably robust for broad spectral absorption.

Our numerical results suggest that the golf-tee pores offer the only augmented J_{MAPD} over the 300-1160 nm wavelength range. This is significant because golf-tee shapes were discovered while using the non-contaminating Al_2O_3 masking agent. If the fabrication process can be precisely tuned to control the shape of the golf-tee pores, these cells could achieve improved solar light trapping and absorption.

The presence of upright pyramids was always found to decrease the cell's net J_{MAPD} , relative to inverted pyramids. The precise arrangement of upright pyramids was also found to significantly influence overall light absorption. Aligning the upright and inverted pyramids in a checkerboard pattern had the most deleterious effect on solar light trapping, reducing J_{MAPD} by 16.8%. Introducing alternating rows of upright and inverted pyramids resulted in a 3.1% reduction of J_{MAPD} . Making all of the pyramids upright resulted in a more modest J_{MAPD} decrease of 2.3%. It is nevertheless noteworthy that this architecture had improved absorption in the 1030-1160 nm range. This structure could be well suited to devices with absorption demands in narrower wavelength ranges, such as infrared photodetectors.

All changes to the depth (side wall angle) of the inverted pyramidal pores resulted in slight overall decreases of J_{MAPD} . The cell with shallower pores had a J_{MAPD} that was 2.3% lower than the reference structure, while the cell with deeper pores had a J_{MAPD} that was 3.0% lower. It is again noteworthy that shallower pyramidal pores provided a higher J_{MAPD} in the 1030-1160 nm range and may be suitable for devices requiring strong infrared light absorption.

Finally, we identified an optimized photonic crystal structure consisting of the best performing golf-tee shaped pores and optimized ARCs. This revealed a J_{MAPD} that was 1.5% higher than the reference structure, for an overall improvement of $0.63 \frac{\text{mA}}{\text{cm}^2}$ in the 300-1190 nm range. This structure's calculated J_{MAPD} of $43.05 \frac{\text{mA}}{\text{cm}^2}$ in the 300-1190 nm range is 93.5% of the J_{MAPD} of a perfect absorber.

Funding. Natural Sciences and Engineering Research Council of Canada; Ontario Research Foundation.

Acknowledgment. This work was supported by the Natural Sciences and Engineering Research Council of Canada and the Ontario Research Foundation (506441).

Disclosures. The authors declare no conflicts of interest.

Data availability. Data underlying the results presented in this paper are available in Refs. [4] and [13].

Supplemental document. See [Supplement 1](#) for supporting content.

References

1. T. Baba, "Slow light in photonic crystals," *Nat. Photonics* **2**(8), 465–473 (2008).
2. S. Bhattacharya and S. John, "Light-trapping by wave interference in intermediate-thickness silicon solar cells," *Opt. Express* **32**(17), 29795–29816 (2024).
3. E. Kane, "Band structure of silicon from an adjusted heine-abarenkov calculation," *Phys. Rev.* **146**(2), 558–567 (1966).
4. M. A. Green, "Improved silicon optical parameters at 25 c, 295 k and 300 k including temperature coefficients," *Prog. Photovoltaics: Res. Appl.* **30**(2), 164–179 (2022).
5. C. Battaglia, A. Cuevas, and S. De Wolf, "High-efficiency crystalline silicon solar cells: status and perspectives," *Energy & Environ. Sci.* **9**(5), 1552–1576 (2016).
6. P. Sinha and A. Wade, "Addressing hotspots in the product environmental footprint of cdtc photovoltaics," in *2017 IEEE 44th Photovoltaic Specialist Conference (PVSC)*, (IEEE, 2017), pp. 2005–2010.
7. K. Sopian, S. Cheow, and S. Zaidi, "An overview of crystalline silicon solar cell technology: Past, present, and future," in *AIP Conference Proceedings*, vol. 1877 (AIP Publishing, 2017).
8. S. Pizzini, "Towards solar grade silicon: Challenges and benefits for low cost photovoltaics," *Sol. Energy Mater. Solar Cells* **94**(9), 1528–1533 (2010).

9. T. Saga, "Advances in crystalline silicon solar cell technology for industrial mass production," *NPG Asia Mater.* **2**(3), 96–102 (2010).
10. M. Powalla, S. Paetel, E. Ahlswede, *et al.*, "Thin-film solar cells exceeding 22% solar cell efficiency: An overview on cdte-, cu (in, ga) se₂-, and perovskite-based materials," *Appl. Phys. Rev.* **5**(4), 041602 (2018).
11. T. Tiedje, E. Yablonovitch, G. D. Cody, *et al.*, "Limiting efficiency of silicon solar cells," *IEEE Trans. Electron Devices* **31**(5), 711–716 (1984).
12. T. Mambri, A. M. Dubois, C. Longeaud, *et al.*, "Photovoltaic yield: Correction method for the mismatch between the solar spectrum and the reference astm g173 1.5g spectrum," *EPJ Photovolt.* **6**, 60701 (2015).
13. NREL, "Reference air mass 1.5 spectra," <https://www.nrel.gov/grid/solar-resource/spectra-am1.5.html/>. Accessed January 13, 2025.
14. D. R. Myers, *The Solar Resource* (Springer New York, New York, NY, 2008), pp. 19–39.
15. H. Horvath, "Atmospheric light absorption—a review," *Atmospheric Environ. Part A. Gen. Top.* **27**(3), 293–317 (1993).
16. S. Bhattacharya and S. John, "Beyond 30% conversion efficiency in silicon solar cells: a numerical demonstration," *Sci. Rep.* **9**(1), 12482 (2019).
17. W. Shockley and H. J. Queisser, "Detailed balance limit of efficiency of p-n junction solar cells," *J. Appl. Phys.* **32**(3), 510–519 (1961).
18. M. A. Green, E. D. Dunlop, M. Yoshita, *et al.*, "Solar cell efficiency tables (version 64)," *Prog. Photovoltaics: Res. Appl.* **32**(7), 425–441 (2024).
19. H. Wu, F. Ye, M. Yang, *et al.*, "Silicon heterojunction back-contact solar cells by laser patterning," *Nature* **635**(8039), 604–609 (2024).
20. H. Lin, M. Yang, X. Ru, *et al.*, "Silicon heterojunction solar cells with up to 26.81% efficiency achieved by electrically optimized nanocrystalline-silicon hole contact layers," *Nat. Energy* **8**(8), 789–799 (2023).
21. J. Maksimovic, J. Hu, S. H. Ng, *et al.*, "Beyond lambertian light trapping for large-area silicon solar cells: Fabrication methods," *Opto-Electron. Adv.* **5**(9), 210086 (2022).
22. S. Almenabawy, Y. Zhang, A. Flood, *et al.*, "Nanometer-mesa inverted-pyramid photonic crystals for thin silicon solar cells," *ACS Appl. Energy Mater.* **5**(11), 13808–13816 (2022).
23. P. Kuang, S. Eyderman, M.-L. Hsieh, *et al.*, "Achieving an accurate surface profile of a photonic crystal for near-unity solar absorption in a super thin-film architecture," *ACS Nano* **10**(6), 6116–6124 (2016).
24. T. Katkus, S. H. Ng, H. Mu, *et al.*, "Bessel-beam direct-write of the etch-mask in a nano-film of alumina for high-efficiency si solar cells," *Advanced Engineering Materials* (2024).
25. L. Jonušauskas, D. Gailevičius, S. Rekštytė, *et al.*, "Mesoscale laser 3d printing," *Opt. Express* **27**(11), 15205–15221 (2019).
26. M.-L. Hsieh, A. Kaiser, S. Bhattacharya, *et al.*, "Experimental demonstration of broadband solar absorption beyond the lambertian limit in certain thin silicon photonic crystals," *Sci. Rep.* **10**(1), 11857 (2020).
27. S. Eyderman, S. John, and A. Deinega, "Solar light trapping in slanted conical-pore photonic crystals: Beyond statistical ray trapping," *J. Appl. Phys.* **113**(15), 154315 (2013).
28. F. M. Korany, M. F. O. Hameed, M. Hussein, *et al.*, "Conical structures for highly efficient solar cell applications," *J. Nanophotonics* **12**(01), 1 (2018).
29. G. Gervinskas, L. Rosa, and S. Juodkazis, "Ion-beam and plasma etching of a conical-pores photonic crystal for thin-film solar cell," in *Micro/Nano Materials, Devices, and Systems*, vol. 8923 (SPIE, 2013), pp. 347–354.
30. S. Bhattacharya and S. John, "Photonic crystal light trapping: Beyond 30% conversion efficiency for silicon photovoltaics," *APL Photonics* **5**(2), 020902 (2020).
31. S. Bhattacharya, I. Baydoun, M. Lin, *et al.*, "Towards 30% power conversion efficiency in thin-silicon photonic-crystal solar cells," *Phys. Rev. Appl.* **11**(1), 014005 (2019).
32. J. Maksimovic, H. Mu, D. Smith, *et al.*, "Laser-patterned alumina mask and mask-less dry etch of si for light trapping with photonic crystal structures," *Micromachines* **14**(3), 550 (2023).
33. J. Maksimovic, H. Mu, M. Han, *et al.*, "Si-cr nano-alloys fabricated by direct femtosecond laser writing," *Materials* **16**(5), 1917 (2023).
34. A. Ingenito, O. Isabella, and M. Zeman, "Experimental demonstration of 4 n² classical absorption limit in nanotextured ultrathin solar cells with dielectric omnidirectional back reflector," *ACS Photonics* **1**(3), 270–278 (2014).
35. M. A. Green, "The path to 25% silicon solar cell efficiency: History of silicon cell evolution," *Prog. Photovoltaics: Res. Appl.* **17**(3), 183–189 (2009).
36. K. Yoshikawa, H. Kawasaki, W. Yoshida, *et al.*, "Silicon heterojunction solar cell with interdigitated back contacts for a photoconversion efficiency over 26%," *Nat. Energy* **2**(5), 17032 (2017).
37. authorship Electromagnetic Template Library Electromagnetic Template Library <https://hipercone.com/doc/emtl/English/html/index.html>, (2025).
38. H. Cui, P. R. Campbell, and M. A. Green, "Optimisation of the back surface reflector for textured polycrystalline si thin film solar cells," *Energy Procedia* **33**, 118–128 (2013).
39. A. Deinega and S. John, "Effective optical response of silicon to sunlight in the finite-difference time-domain method," *Opt. Lett.* **37**(1), 112–114 (2012).
40. A. Deinega, I. Valuev, B. Potapkin, *et al.*, "Minimizing light reflection from dielectric textured surfaces," *J. Opt. Soc. Am. A* **28**(5), 770–777 (2011).